## Electronic Supplementary Information

# A novel method for the green synthesis of biobased hexamethylene-1,6-dicarbamate

Yunhan Bai [a], Dule Huhe [a], Xinyu Du [a], Yucong Song [a,b], Xiaoshu Ding [a,b,*], Dongsheng Zhang [a,b], Xinqiang Zhao [a,b], Yanji Wang [a,b,*]

[a] Hebei Provincial Key Laboratory of Green Chemical Technology and High Efficient Energy Saving, School of Chemical Engineering and Technology, Hebei University of Technology, Tianjin, 300401, China

[b] Tianjin Key Laboratory of Inherent Safety Chemical Process, School of Chemical Engineering, Hebei University of Technology, Tianjin, 300401, China

* Corresponding author: Yanji Wang; Xiaoshu Ding

E-mail addresses: yjwang@hebut.edu.cn (Yanji Wang); dxshu@hebut.edu.cn (Xiaoshu Ding)

## 1 Product qualitative analysis and catalyst characterization methods

The nuclear magnetic resonance spectrometer was tested using AVANCE400, which Bruker BioSpin AG in Switzerland manufactures. The Fourier transform infrared spectrometer is the Nicolet NEXUS 470. The automatic elemental analyzer is Flash EA 1112 from the United States, with an accuracy of ≤0.30%. High-resolution mass spectrometer (HRMS) is a Compact produced by Bruker Scientific Instruments that ensures accuracy of more than 1 ppm through automatic calibration. The melting point instrument is WRS-3A, with a heating rate of 1 °C/min. Each substance is tested three times, and the average value represents the final melting point.

The phase analysis of the catalyst was carried out by the D8 Discover X-ray diffractometer produced by Brook, Germany. The scanning range was set from 10° to 90° with a scanning rate of 6 °/min. TEM was conducted using the TalosF200S instrument from FEI, USA. Electron paramagnetic resonance (EPR) spectroscopy was recorded using the BRUKE EMXPLUS spectrometer at room temperature. The operating frequency and power were 9.80 GHz and 20.13 W, respectively. The surface elemental chemical states of the catalyst were measured using an X-ray Photoelectron Spectrometer (XPS) model Escablab 250Xi, manufactured by Thermo Fisher Scientific Inc. of the United States. The C 1s peak at 284.8 eV was used to calibrate all binding energies. $H_2$ temperature programmed reduction ($H_2$-TPR) measurements were conducted on the AutoChem II-2920 reactor. Before the measurement, the sample (100 mg) was degassed at 200 °C under an Ar flow (50 mL/min) for 1 h. Then cool it to 50 °C. Subsequently, it was heated from 50 °C to 450 °C at a rate of 10 °C/min while introducing a flow of 10% $H_2$/Ar mixture. In situ FT-IR analysis was performed using a Thermo-NICOLET NEXUS-470 spectrometer equipped with an MCT detector, which had a resolution of 4 $cm^{-1}$. A sample weighing 5 mg was pressed and placed in an in-situ transmission cell (with a $CaF_2$ window), and then subjected to hydrogen treatment at 170 °C for 30 min with a 20 mL/min $H_2$ flow rate. Then cool to 50 °C, switch the $H_2$ to He flow, blow out for 1 h, and record the background spectrum. Then, the ethanol solution of FDC was dropped in situ onto the sample surface. The He gas was

introduced to maintain the condition for 1 h, and then the infrared spectrum in the range of 1450-1800 $cm^{-1}$ was collected.

## 2 Density functional theory (DFT) calculations

The Pt (111) structure was optimized to create a five-layer metal, and a 6*8 cell expansion was performed in the xy direction. The optimized molecules were adsorbed onto the surface of Pt (111), and the adsorption energy was calculated. The dynamic calculations were performed using the CP2K package (version 2023.2), based on Perdew-Burke-Ernzerhof (PBE) functional and a hybrid Gaussian/Plane-Wave scheme (GPW).[1] The GTH pseudopotentials were chosen to describe the core electrons.[2] The wave functions were expanded in optimized double-ζ Gaussian basis sets, and the plane waves were expanded with a cutoff energy of 400 Rydberg. Dispersion correction was applied in all calculations with the DFT-D3 method.[3] The transition state and activation energy were determined using the Dimer method. The activation energy corresponds to the energy difference between the optimized transition state and the reactant state. The binding energy ($E_{BE}$) was calculated using: $E_{BE} = E_{slab+adsorbate} - (E_{slab}+E_{gas})$.

## 3 Qualitative analysis of 2-hydroxy-hexamethylene-1,6-dicarbamate (HHDC)

HHDC is a tasteless white crystal that is easily soluble in organic solvents such as dimethyl sulfoxide. It is also easily soluble in water, has a melting range of 73.8-73.9 °C, and has a molecular weight of 248.1372. The nuclear magnetic spectra of HHDC are shown in Fig. S1 and Fig. S2. The $^{1}$H NMR (400 MHz, DMSO) δ: 7.07 (s, 1H), 6.99 (s, 1H), 4.55 (d, J = 8.0 Hz, 1H), 3.50 (s, 6H), 3.40 (s, 1H), 2.96-2.87 (m, 4H), 1.38-1.32 (m, 4H), 1.24-1.18 (m, 2H); $^{13}$C NMR (100 MHz, DMSO) δ: 157.05, 156.86, 69.18, 51.41, 51.31, 47.05, 40.50, 34.23, 29.78, 22.58. In the HRMS spectrum of HHDC (Fig. S3), m/z = 249.1446 $[M+H]^+$, the theoretical value is 249.1445; m/z = 271.1264 $[M+Na]^+$, the theoretical value of 271.1264. In the FTIR spectrum of HHDC (Fig. S4), the absorption

peak at 3410 $cm^{-1}$ corresponds to the stretching vibration of the alcohol hydroxyl group. The adsorption peak at 3350$cm^{-1}$ corresponds to the stretching vibration of the N-H bond. The peaks at 2914$cm^{-1}$ and 2866$cm^{-1}$ represent the symmetric and antisymmetric stretching vibrations of saturated C-H bonds. The characteristic adsorption peak of the C=O functional group is at 1689 $cm^{-1}$. The bending vibration peak of secondary amine is at 1531 $cm^{-1}$. The peak at 1477 $cm^{-1}$ represents the bending vibration of methylene. The stretching vibration peaks of C-O-C are at 1267 $cm^{-1}$ and 1056 $cm^{-1}$. The absorption peak at 1145$cm^{-1}$ corresponds to the skeletal vibration of C-C-C. The theoretical values of elemental analysis for HHDC are as follows: C, 48.37%; H, 8.120%; N, 11.29%. The measured values are as follows: C, 47.91%; H, 7.638%; N, 12.70%.

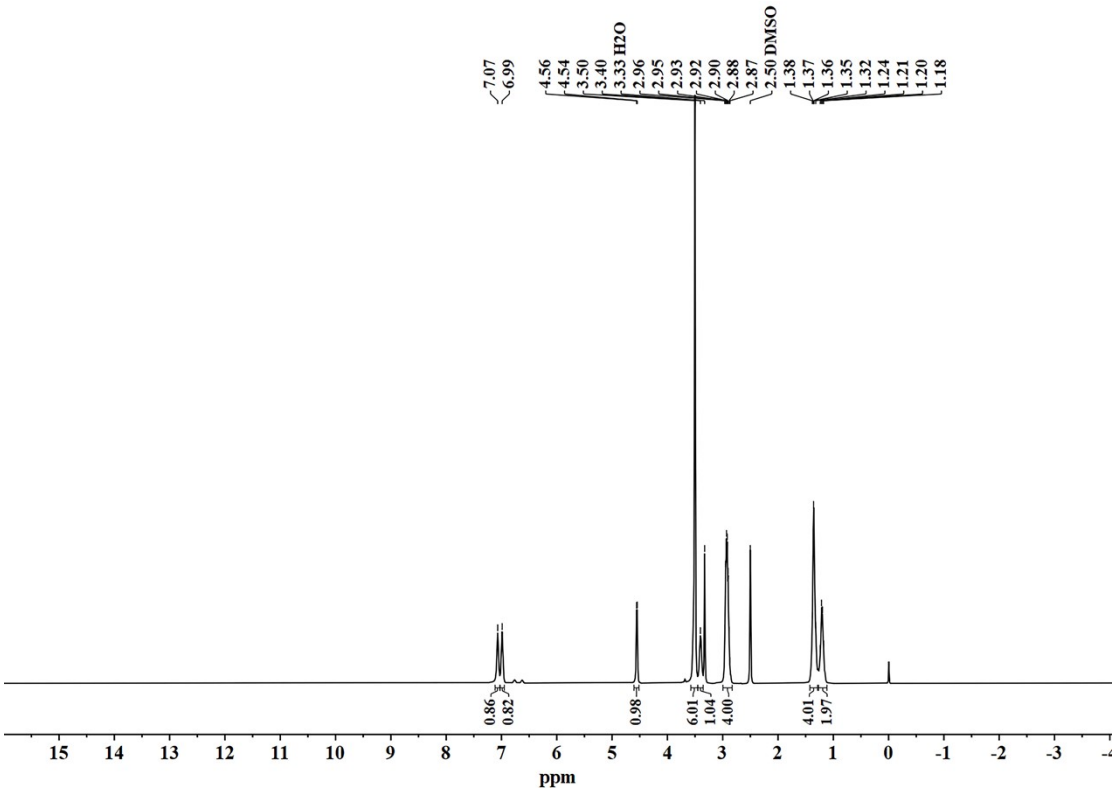


**Fig. S1** $^{1}H$ NMR of HHDC.

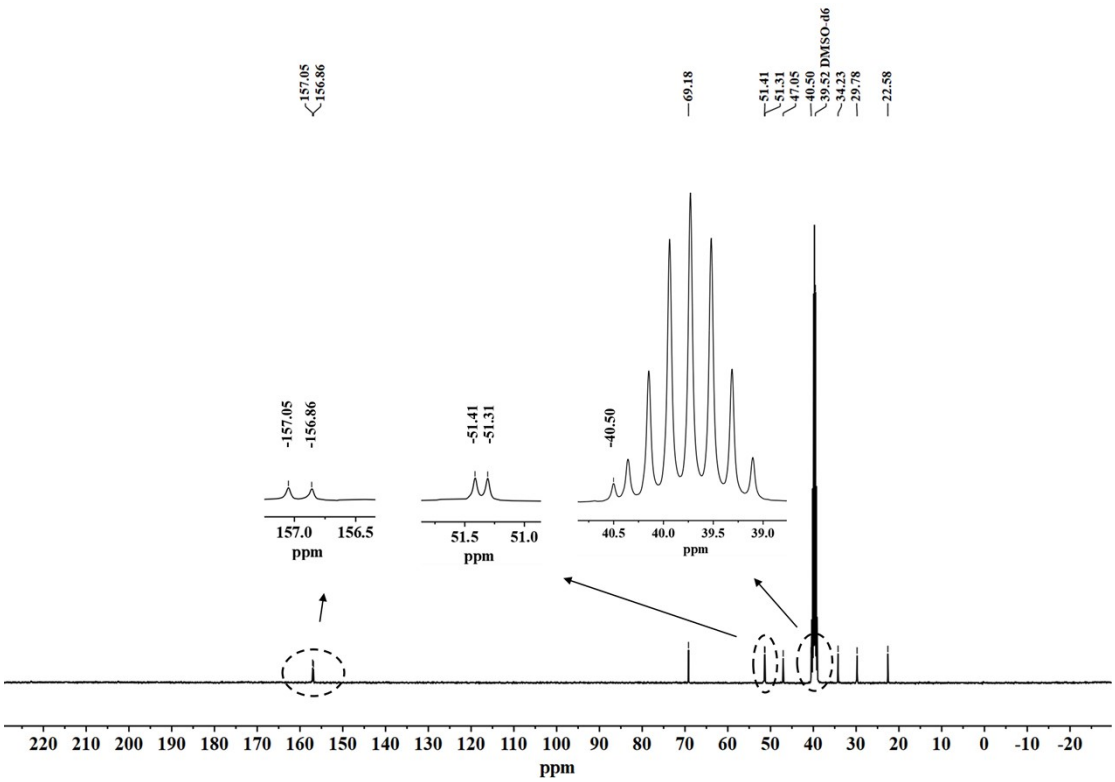


**Fig. S2** $^{13}C$ NMR of HHDC.

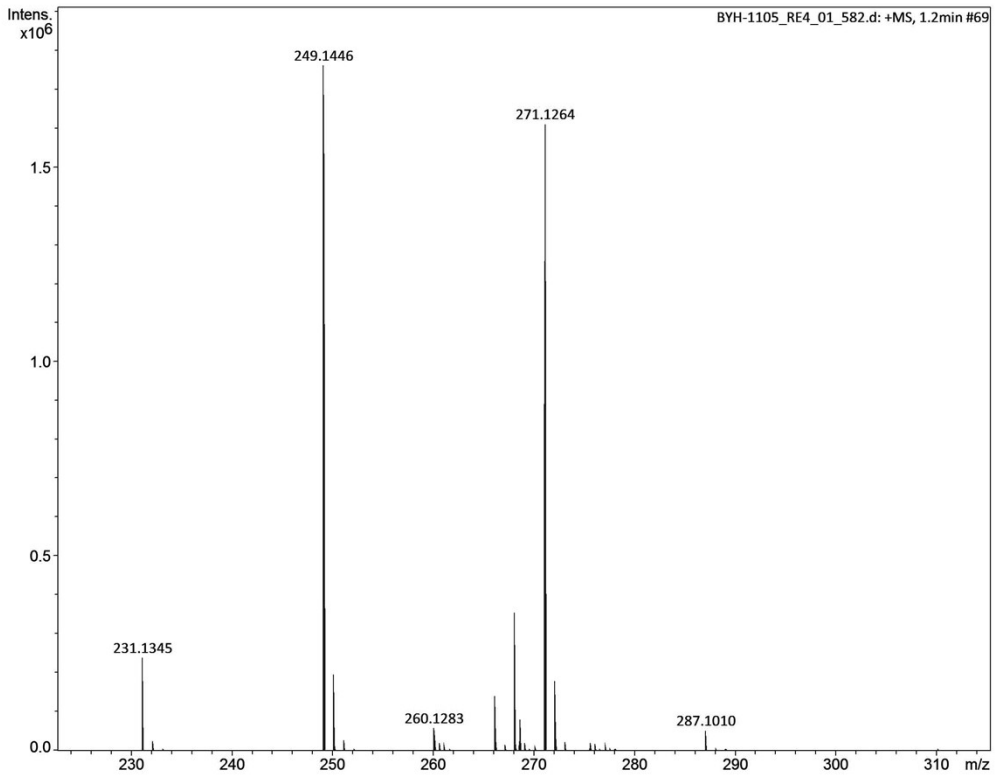


**Fig. S3** HRMS of HHDC.

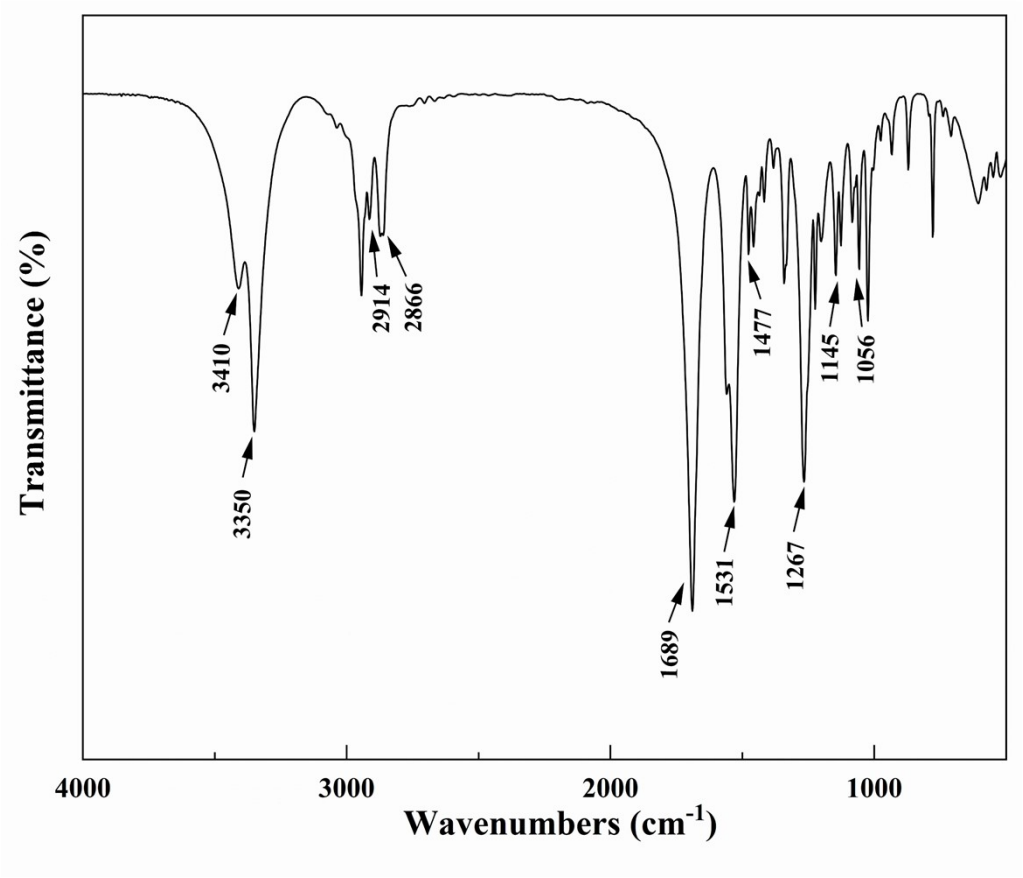


**Fig. S4** FTIR of HHDC.

## 4 Catalyst characterization results

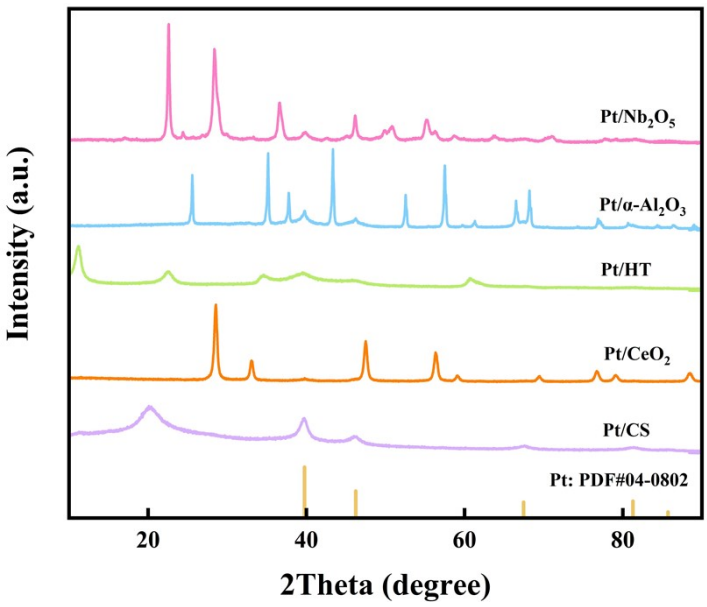


**Fig. S5** XRD patterns of Pt-based catalysts on different supports.

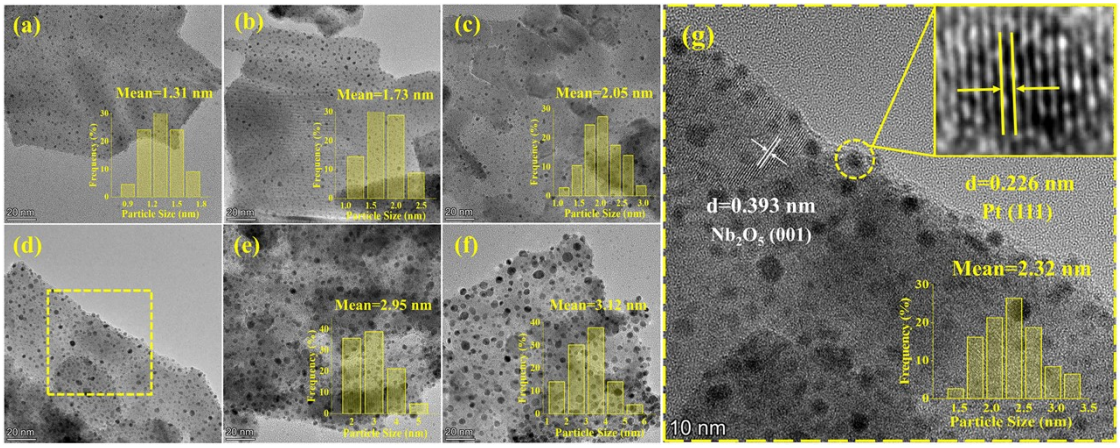


**Fig. S6.** TEM images of $Pt/Nb_2O_5$ catalysts with different Pt loadings (a) 1wt.%, (b) 3wt.%, (c) 5wt.%, (d) 7wt.%, (e) 10wt.%, (f) 15wt.%. (g) An enlarged view of the yellow frame is in (d).

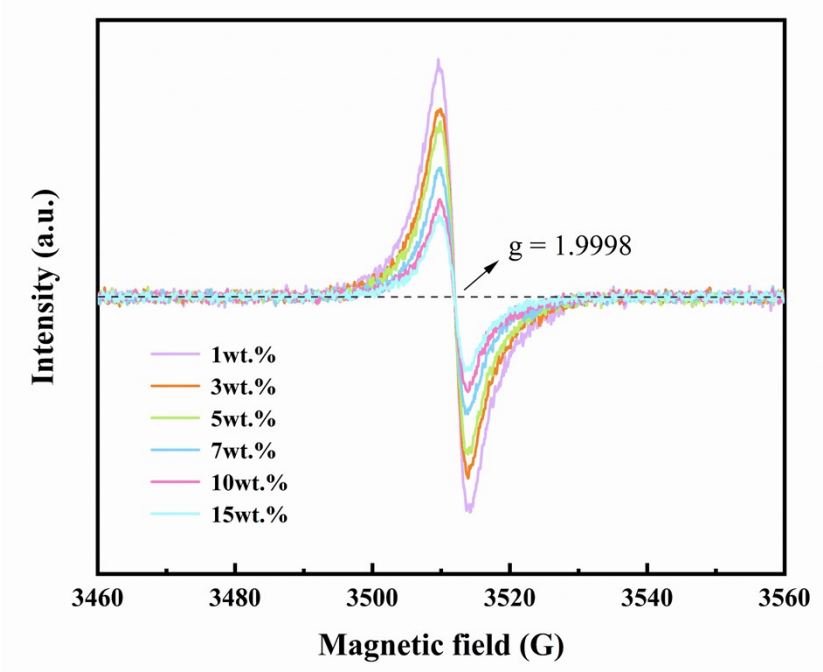


**Fig. S7.** Electron paramagnetic resonance (EPR) spectra of $Pt/Nb_2O_5$ catalysts with different Pt loadings.

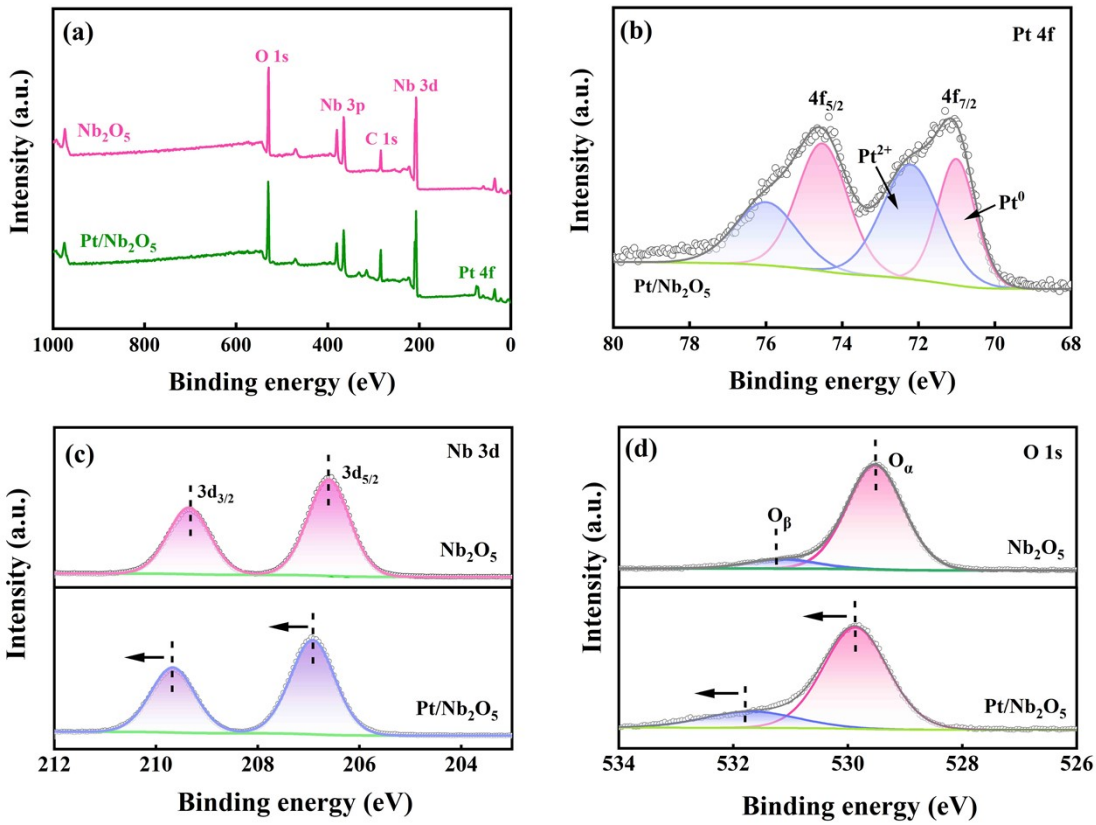


Fig. S8 XPS analysis of samples. (a) Survey spectra of $Nb_2O_5$ and 7%Pt/$Nb_2O_5$. (b) Pt 4f peaks of 7%Pt/$Nb_2O_5$. (c) Nb 3d and (d) O 1s peaks of $Nb_2O_5$ and 7%Pt/$Nb_2O_5$.

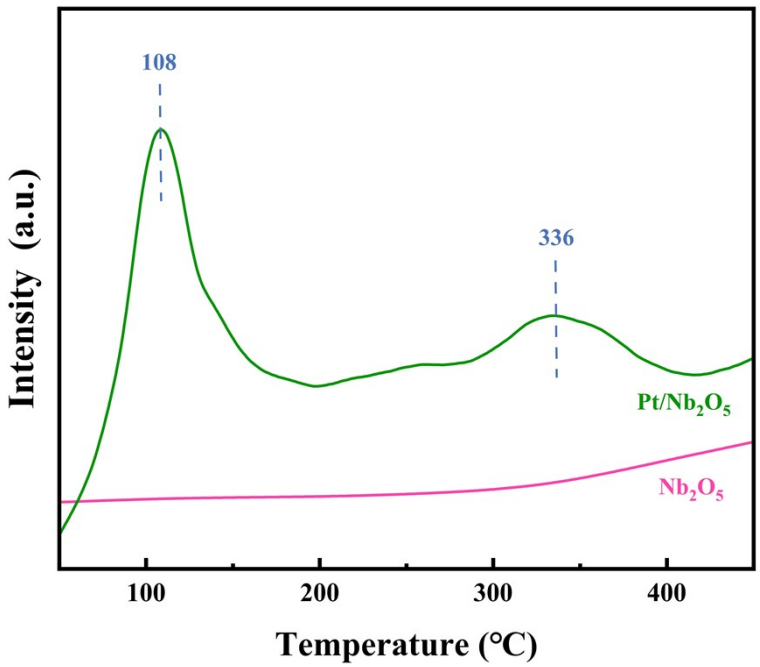


**Fig. S9** $H_2$-TPR spectra obtained from $Nb_2O_5$ and 7%Pt/$Nb_2O_5$.

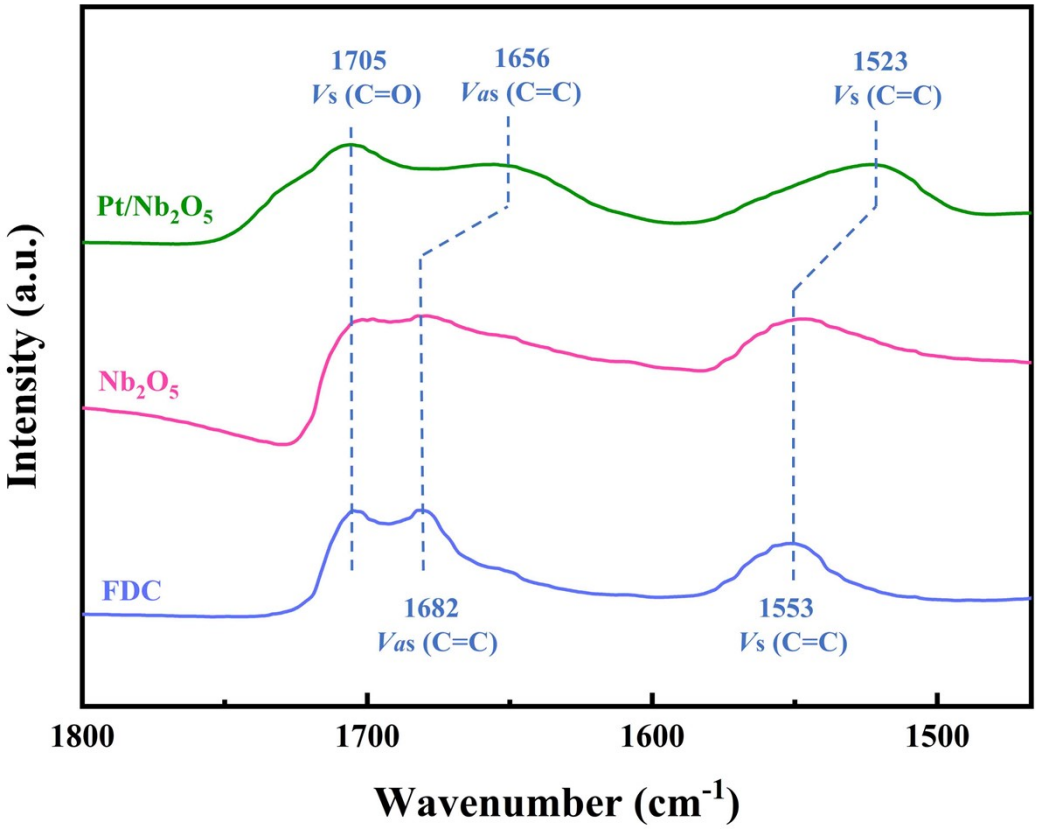


**Fig. S10.** The in situ FTIR spectra for absorption of FDC on $Nb_2O_5$ and 7%Pt/$Nb_2O_5$ and the FTIR spectra for standard FDC.

## 5 Reduction of various substrates

**Table S1** Reduction of different substrates on 5%Pt/$Nb_2O_5$ catalyst.

| Entry | Substrate | Conversion (%) | Yield (%) | | |
|---|---|---|---|---|---|
| | | | THFDC | HHDC | HDC |
| 1 | FDC | > 99.9 | 28.4 | 56.5 | 9.66 |
| 2 | THFDC | - | - | - | - |
| 3 | HHDC | - | - | - | - |

Reaction conditions: FDC (0.2 g), 5%Pt/$Nb_2O_5$ (0.1 g), Solvent ($V_{EtOH}$: $V_{H2O}$=1: 1, 20 mL), $H_2$ (3 MPa), 170 °C, 3 h. Defined 0 h when the temperature reached the specified temperature.

## 6 DFT calculation results

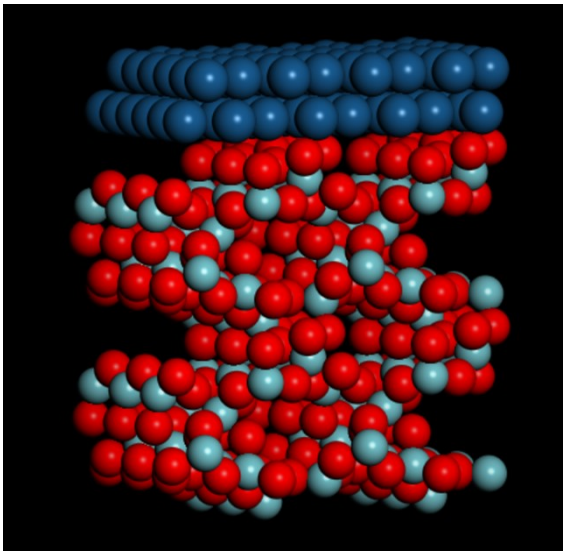

Fig. S11 Two layers of Pt (111) are adsorbed on the surface of one layer of $Nb_2O_5$ (001). (Atom legend: Pt, light blue; O, red; H, cyan.)

The change in the energy barrier of the reaction, as derived from DFT, indicates that the first addition of H is more kinetically and thermodynamically favored at the C3 position (Table S2, Fig. S12). The hydrogenation of oxygen atoms has a high energy level. The reaction energy barrier for FDC* direct ring-opening is very high, indicating that FDC* ring-opening is not competitive compared to FDC* hydrogenation.

**Table S2** The reaction energy barrier (ΔE) and activation energy ($E_a$) of the elementary reaction steps of FDC* ring-saturation and ring-opening on Pt (111) surface are calculated by DFT.[a]

| Entry | Elementary step | ΔE (eV) | $E_a$ (eV) |
|---|---|---|---|
| 1 | FDC*+H*↔FDC-1* | 0.76 | - |
| 2 | FDC*+H*↔FDC-2* | 0.52 | - |
| 3 | FDC*+H*↔FDC-3* | -0.47 | 0.12 |
| 4 | FDC*↔FDC-ro* | 2.57 | - |

[a] FDC* and FDC-x* (x=1-5) represent the adsorbed FDC and partially hydrogenated intermediates on the Pt (111) surface, respectively. Here, x represents the order of attack positions of H* (marked in Fig. 11). For instance, FDC-3* represents an intermediate formed by hydrogenation at the C3 site of the FDC*. FDC-ro* represents the ring-opening intermediate resulting from the cleavage of the O1-C2(5) bond of the FDC*.

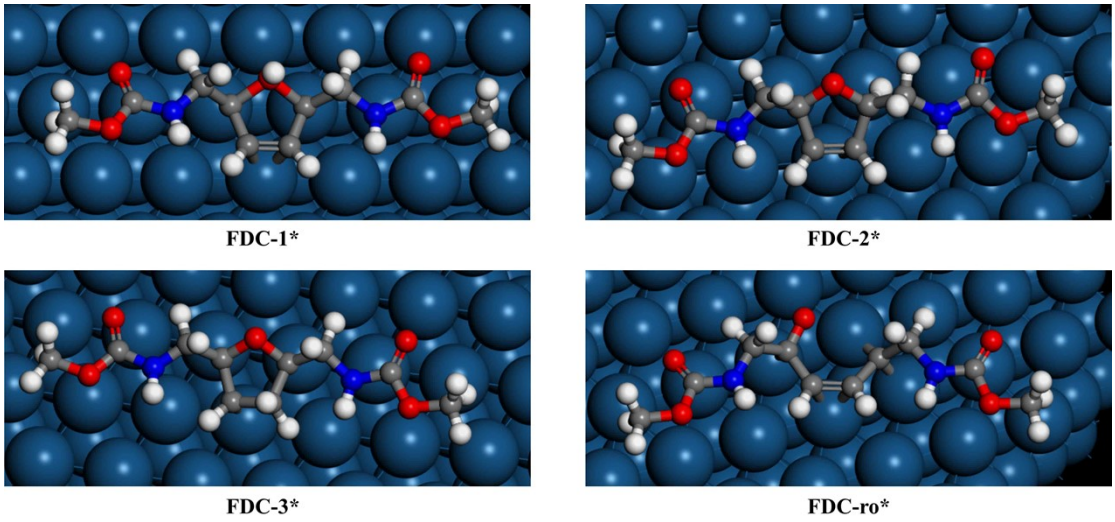


**Fig. S12** Calculated structures of FDC* ring-saturation and ring-opening on Pt (111) surface. (Atom legend: Pt, light blue; C, gray; O, red; N, blue; H, white.)

There are several possible products for the subsequent reaction of FDC-3* with the second hydrogen atom (Table S3, Fig. S13). DFT calculations show that the second H atom has a high reaction energy barrier for attacking the other three C positions in the furan ring and cleaving the O1-C2(5) bond. In particular, the high reaction energy barrier required for cleaving the O1-C5 bond to form FDC-3-ro# indicates that the reaction is difficult to carry out. Therefore, the subsequent reaction will not consider the cleavage of the O1-C5 bond. In contrast, the reaction energy barrier of FDC-31* is the lowest, indicating that hydrogenation on oxygen is more favorable than carbon.

**Table S3** The reaction energy barrier (ΔE) and activation energy ($E_a$) of the elementary reaction steps of FDC-3* ring-saturation and ring-opening on Pt (111) surface are calculated by DFT.[a]

| Entry | Elementary step | ΔE (eV) | $E_a$ (eV) |
|---|---|---|---|
| 1 | FDC-3*+H*↔FDC-31* | 0.28 | 0.41 |
| 2 | FDC-3*+H*↔FDC-32* | 0.71 | - |
| 3 | FDC-3*+H*↔FDC-34* | 1.50 | - |
| 4 | FDC-3*+H*↔FDC-35* | 0.75 | - |
| 5 | FDC-3*↔FDC-3-ro* | 1.28 | - |
| 6 | FDC-3*↔FDC-3-ro#* | 3.17 | - |

[a] FDC-x* (x=1-5) represents the partially hydrogenated intermediates that are adsorbed on the Pt (111) surface, where x represents the order of attack positions of H* (marked in Fig. 11). For instance, FDC-31* represents the adsorption intermediate formed by sequential hydrogenation at the C3 and O1 sites of FDC*. FDC-3-ro* and FDC-3-ro#* represent the ring-opening intermediates of the O1-C2 bond and O1-C5 bond cleavage in FDC-3*, respectively.

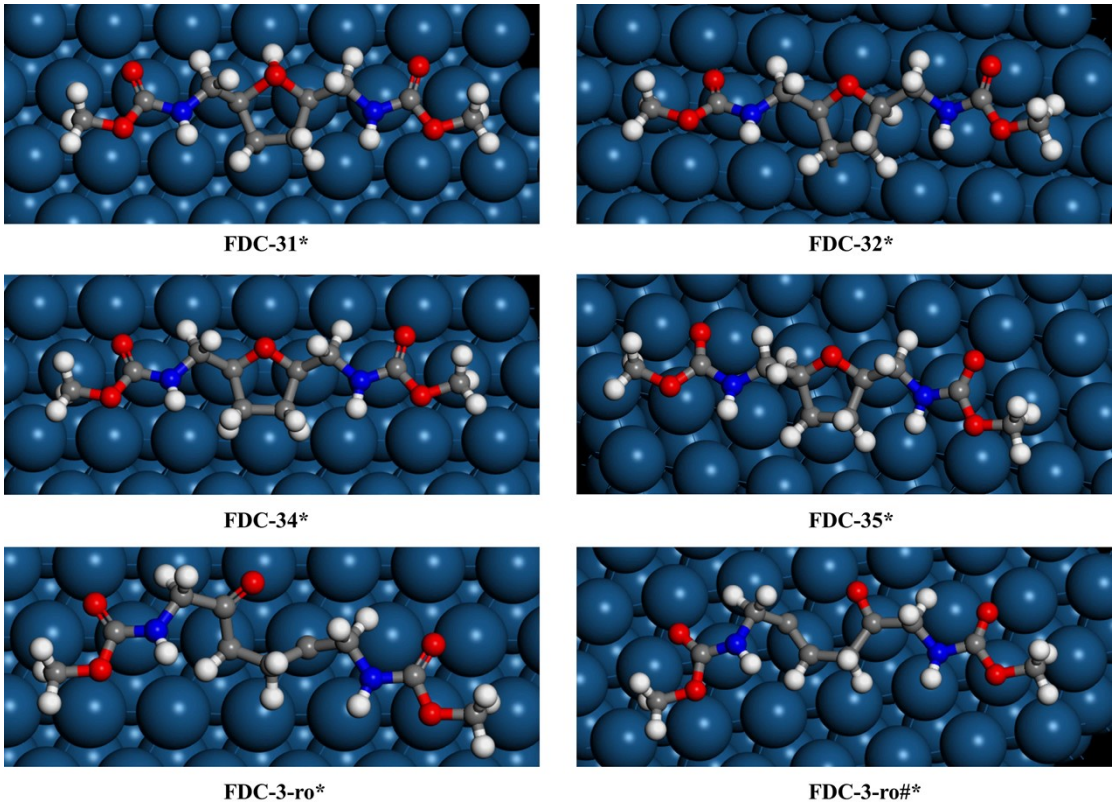


**Fig. S13** Calculated structures of FDC-3* ring-saturation and ring-opening on Pt (111) surface. (Atom legend: Pt, light blue; C, gray; O, red; N, blue; H, white.)

The DFT derivative reaction energy barriers of FDC-31* for H addition and ring-opening indicate that the energy barrier for ring-opening to FDC-31-ro* is lower than that for ring-saturation. This suggests that C-O bond cleavage is kinetically more favorable than ring-saturation on the Pt (111) surface (Table S4, Fig. S14).

**Table S4** The reaction energy barrier (ΔE) and activation energy ($E_a$) of the elementary reaction steps of FDC-31* ring-saturation and ring-opening on Pt (111) surface are calculated by DFT.[a]

| Entry | Elementary step | ΔE (eV) | $E_a$ (eV) |
|---|---|---|---|
| 1 | FDC-31*+H*↔FDC-312* | 1.35 | - |
| 2 | FDC-31*+H*↔FDC-314* | 0.96 | - |
| 3 | FDC-31*+H*↔FDC-315* | 0.72 | - |
| 4 | FDC-31*↔FDC-31-ro* | 0.32 | 0.44 |

[a] FDC-x* (x=1-5) represents the partially hydrogenated intermediates that are adsorbed on the Pt (111) surface, where x represents the order of attack positions of H* (marked in Fig. 11). For instance, FDC-312* represents the adsorption intermediate formed by sequential hydrogenation at the C3, O1, and C2 sites of FDC*. FDC-31-ro* represents the ring-opening intermediates of O1-C2 bond cleavage in FDC-31*.

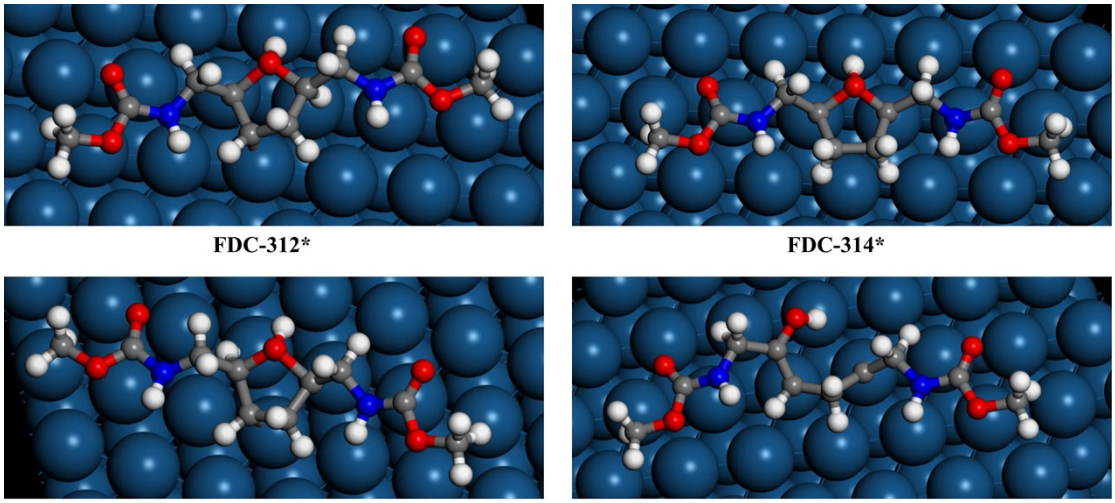


**Fig. S14** Calculated structures of FDC-31* ring-saturation and ring-opening on Pt (111) surface. (Atom legend: Pt, light blue; C, gray; O, red; N, blue; H, white.)

**Table S5** The reaction energy barrier (ΔE) and activation energy ($E_a$) of the elementary reaction steps of FDC-31-ro* hydrogenation on Pt (111) surface are calculated by DFT.[a]

| Entry | Elementary step | ΔE (eV) | $E_a$ (eV) |
|---|---|---|---|
| 1 | FDC-31-ro*+H*↔FDC-31-ro-2* | -1.10 | 0.15 |
| 2 | FDC-31-ro-2*+H*↔FDC-31-ro-24* | -0.47 | 0.14 |
| 3 | FDC-31-ro-24*+H*↔FDC-31-ro-245* | -0.06 | 0.15 |

[a] FDC-31-ro* represent the ring-opening intermediates of O1-C2 bond cleavage in FDC-31*. FDC-31-ro-2* represents the C2 hydrogenation intermediate of FDC-31-ro*. FDC-31-ro-24* represents the C4 hydrogenation intermediate of FDC-31-ro-2*. FDC-31-ro-245* represents the C5 hydrogenation intermediate of FDC-31-ro-24*.

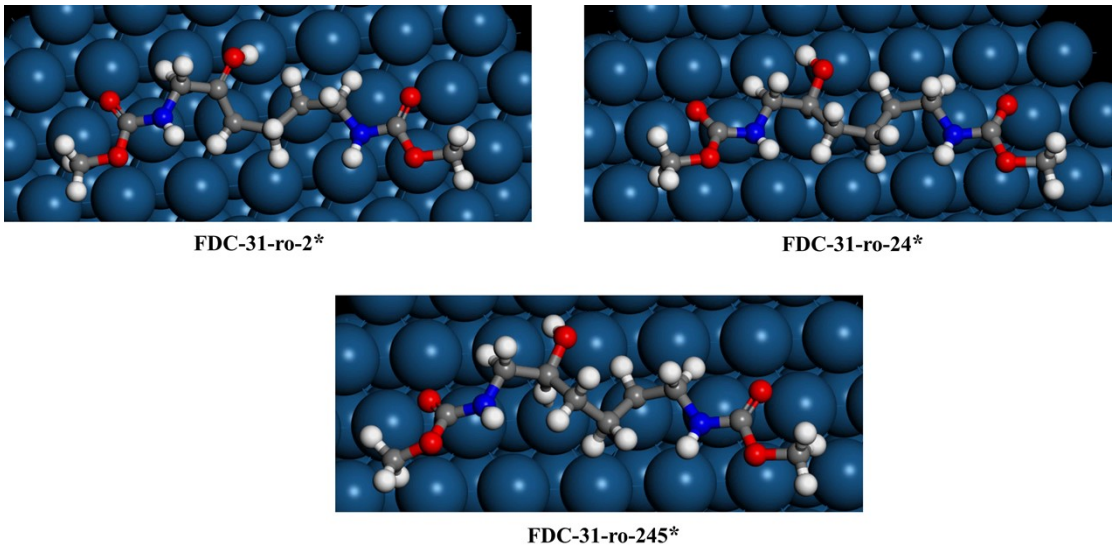


**Fig. S15** Calculated structures of FDC-31-ro* hydrogenation on Pt (111) surface. (Atom legend: Pt, light blue; C, gray; O, red; N, blue; H, white.)

**Table S6** The reaction energy barrier (ΔE) and activation energy ($E_a$) of the elementary reaction steps of Y* hydrogenation and deoxidation on Pt (111) surface are calculated by DFT.[a]

| Entry | Elementary step | ΔE (eV) | $E_a$ (eV) |
|---|---|---|---|
| 1 | Y*↔MHDC*+OH* | -0.16 | 0.35 |
| 2 | Y*+$H_2O$*↔MHDC-a*+$H_2O$*+OH* | -0.19 | 0.17 |
| 3 | Y*+$H_2O$#*↔MHDC-b*+$H_2O$#*+OH* | -0.27 | 0.21 |
| 4 | Y*+H*↔HHDC* | -0.44 | 0.13 |

[a] Y* represents the ring-opening hydrogenation intermediate, FDC-31-rop-125*. $H_2O$* and $H_2O$#* represent $H_2O$ molecules as hydrogen bond donors and acceptors, respectively. MHDC* represents the deoxygenated intermediate of direct cleavage of the C5-O1 bond in Y* without $H_2O$. MHDC-a* and MHDC-b* represent the deoxygenated intermediates of C5-O1 bond cleavage when $H_2O$ acts as a hydrogen bond donor and acceptor to form hydrogen bonds with Y*, respectively. HHDC* represents the adsorbed HHDC.

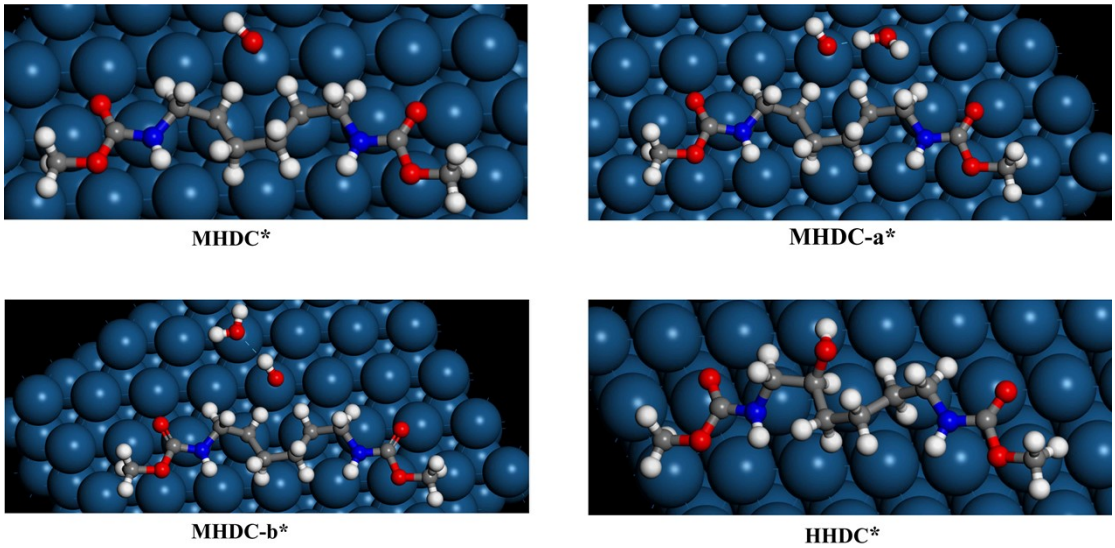


**Fig. S16** Calculated structures of the deoxidation and hydrogenation reaction of Y*. (Atom legend: Pt, light blue; C, gray; O, red; N, blue; H, white.)

**Table S7** The reaction energy barrier (ΔE) and activation energy ($E_a$) of the elementary reaction steps of MHDC-a* hydrogenation on Pt (111) surface are calculated by DFT.[a]

| Entry | Elementary step | ΔE (eV) | $E_a$ (eV) |
|---|---|---|---|
| 1 | MHDC-a*+H*↔MHDC-a-2* | 0.21 | 0.37 |
| 2 | MHDC-a-2*+H*↔HDC* | -0.51 | 0.18 |

[a] MHDC-a* represents the deoxygenated intermediates of C5-O1 bond cleavage when $H_2O$ acts as a hydrogen bond donor to form hydrogen bonds with Y*. MHDC-a-2* represents the intermediate formed by hydrogenating MHDC-a at the C2 position, and HDC* represents the adsorbed HDC.

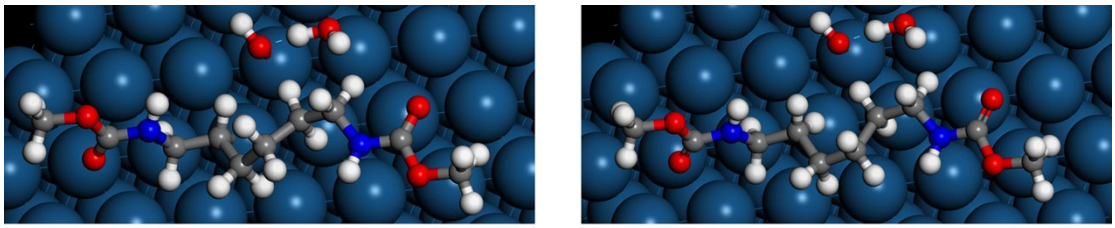


**Fig. S17** Calculated structure of the generation reaction of HDC*. (Atom legend: Pt, light blue; C, gray; O, red; N, blue; H, white.)

Based on Table S3 and Fig. S13, it can be observed that the hydrogenation of the remaining carbon atoms in the furan ring of FDC-3* predominantly occurs at the C2 position, resulting in the formation of FDC-32*. Next, the reaction energy barriers for subsequent hydrogenation and ring-opening of FDC-32* were calculated (Table S8, Fig. S18). DFT calculations show that the reaction energy barrier for the third H atom attacking the C5 position in the furan ring is higher than that of the C4 position, indicating a preference for adding the third H atom to the C4 position. The high reaction energy barrier required for the cleavage of the O1-C5 bond in FDC-32* indicates that carrying out the reaction is difficult.

**Table S8** The reaction energy barrier (ΔE) of the elementary reaction steps of FDC-32* ring-saturation and ring-opening on Pt (111) surface are calculated by DFT.[a]

| Entry | Elementary step | ΔE (eV) |
|---|---|---|
| 1 | FDC-32*+H*↔FDC-324* | 0.24 |
| 2 | FDC-32*+H*↔FDC-325* | 0.28 |
| 3 | FDC-32*↔FDC-32-ro* | 0.34 |

[a] FDC-x* (x=1-5) represents the partially hydrogenated intermediates that are adsorbed on the Pt (111) surface, where x represents the order of attack positions of H* (marked in Fig. 11). For instance, FDC-324* represents the adsorption intermediate formed by sequential hydrogenation at the C3, C2 and C4 sites of FDC*. FDC-32-ro* represents the ring-opening intermediates of O1-C2 bond cleavage in FDC-32*.

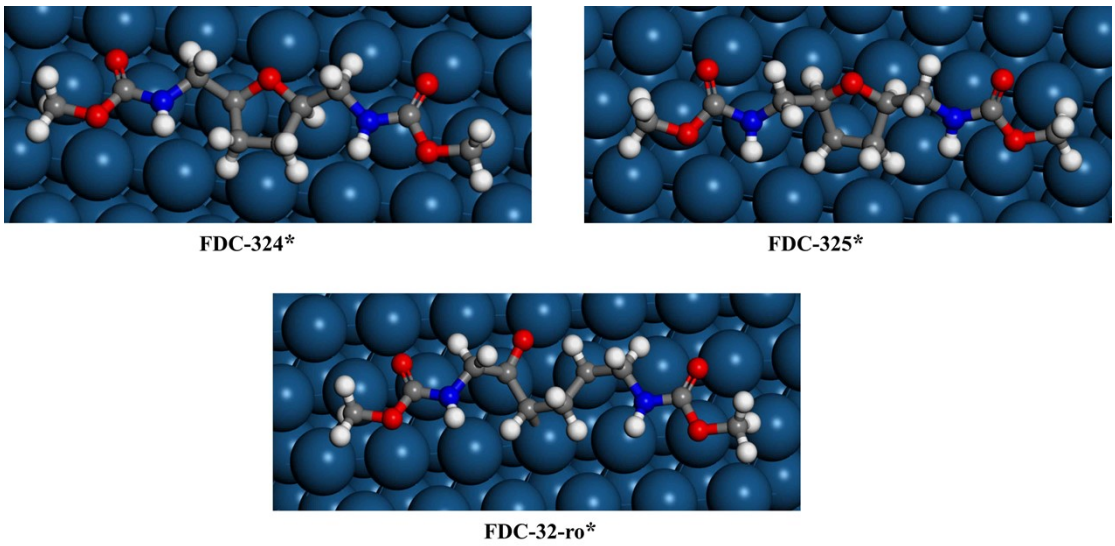


**Fig. S18** Calculated structures of FDC-32* hydrogenation and ring-opening. (Atom legend: Pt, light blue; C, gray; O, red; N, blue; H, white.)

The DFT-derived reaction energy barriers for H-addition and ring-opening reactions of FDC-324* indicate that the direct ring-opening reaction has a very high energy barrier, making it less competitive compared to the hydrogenation reaction of FDC-324* (Table S9, Fig. S19). Therefore, FDC-324* is preferentially hydrogenated at the C5 position to form THFDC*.

**Table S9** The reaction energy barrier (ΔE) of the elementary reaction steps of FDC-324* hydrogenation and ring-opening on Pt (111) surface are calculated by DFT.[a]

| Entry | Elementary step | ΔE (eV) |
|---|---|---|
| 1 | FDC-324*+H*↔THFDC* | -0.43 |
| 2 | FDC-324*↔FDC-324-ro* | 0.09 |

[a] FDC-x* (x=1-5) represents the partially hydrogenated intermediates that are adsorbed on the Pt (111) surface, where x represents the order of attack positions of H* (marked in Fig. 11). For instance, FDC-324-ro* represents the ring-opening intermediates of O1-C2 bond cleavage in FDC-324*.

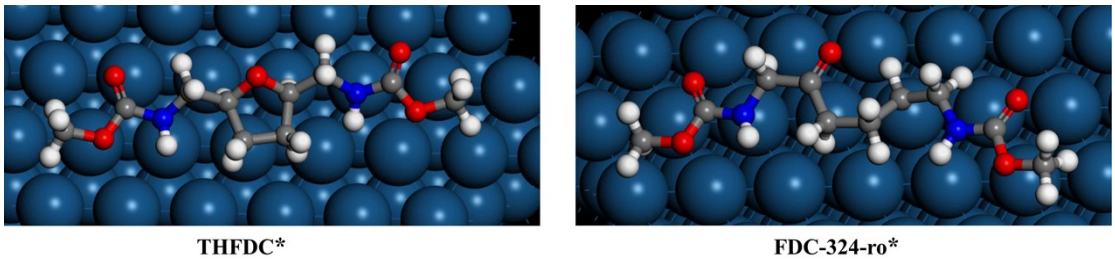


**Fig. S19** Calculated structures of FDC-324* hydrogenation and ring-opening. (Atom legend: Pt, light blue; C, gray; O, red; N, blue; H, white.)

The reaction pathways of FDC hydrogenolysis, deoxidation, and ring-saturation are proposed based on the above information, as shown in Fig. S20. An H atom initially attacks the C3 position of FDC*, and the resulting FDC-3* serves as a reactive intermediate for hydrogenation and ring-opening. The THFDC is formed by the sequential hydrogenation of the carbon atoms on the furan ring in the order of C3, C2, C4, and C5. Due to the high reaction energy barrier associated with the ring-opening of FDC-32* and FDC-324*, the possibility of ring-opening occurring once such substances are formed is very low. Therefore, as an essential intermediate, the reaction of FDC-3* determines both the reaction trajectory and selectivity of the entire system. The O1 atom of FDC-3* is hydrogenated, which facilitates breaking the C2-O1 bond. After ring-opening and subsequent hydrogenation, it transforms into a more stable FDC-31-rop-245 (Y*). Y* is easily hydrogenated to form HHDC. When the oxygen of the hydroxyl group in Y* acts as a hydrogen bond acceptor and combines with $H_2O$ in the system to form a hydrogen bond, the electron density in the C-OH bond is reduced, thereby promoting its cleavage, and then further hydrogenation occurs to form HDC*.

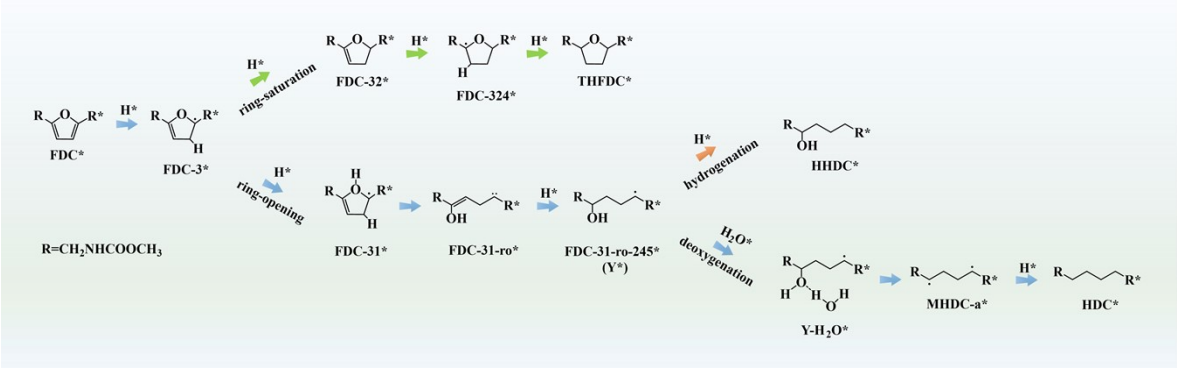


**Fig. S20** The reaction pathways of FDC hydrogenolysis, deoxidation, and ring-saturation.

## References

1 J. V. Vondele, M. Krack, F. Mohamed, M. Parrinello, T. Chassaing and J. Hutter, *Comput. Phys. Commun.*, 2005, **167**, 103-128.

2 C. Hartwigsen, S. Goedecker and J. Hutter, *Phys. Rev. B*, 1998, **58**, 3641-3662.

3 S. Grimme, S. Ehrlich and L. Goerigk, *J. Comput. Chem.*, 2011, **32**, 1456-1465.